Supporting Information

Synthetic Model of the [Mn_3CaO_4] Cubane Core of the Oxygen-Evolving Complex of Photosystem II

Shreya Mukherjee,[1] Jamie A. Stull,[2] Junko Yano,[3] Theocharis C. Stamatatos,[1] Konstantina Pringouri,[1] Troy A. Stich,[2] Khalil A. Abboud,[1] R. David Britt,[2] Vittal K. Yachandra,[3] and George Christou[1*]

Crystal Structure of Complex 1

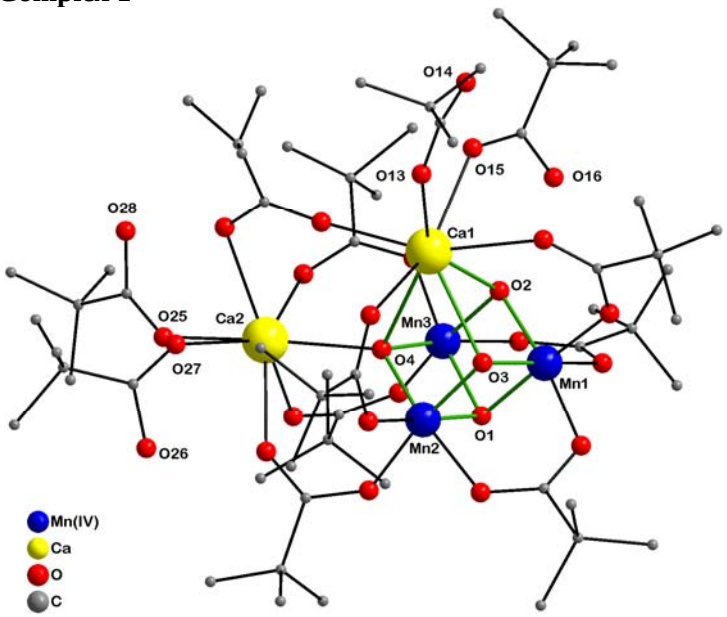

Figure S1. Partially labeled PovRay representation of **1**. Hydrogen atoms have been removed for clarity.

X-ray crystallography. Data were collected at 173 K on a Siemens SMART PLATFORM equipped with a CCD area detector and a graphite monochromator utilizing MoK_α radiation (λ = 0.71073 Å). Suitable crystal of **1** was attached to glass fiber using silicone grease and transferred to a goniostat, where it was cooled to 173 K for data collection. Cell parameters were refined using up to 8192 reflections. A full sphere of data (1850 frames) was collected using the ω-scan method (0.3° frame width). The first 50 frames were re-measured at the end of data collection to monitor instrument and crystal stability (maximum correction on *I* was <1 %). Absorption corrections by integration were applied based on measured indexed crystal faces.

The structure was solved by the Direct Methods in *SHELXTL6* (1), and refined using full-matrix least squares. The non-H atoms were treated anisotropically, whereas the hydrogen atoms were calculated in ideal positions and were riding on their respective carbon atoms. The Mn_3Ca_2 cluster crystallizes without any solvent molecule in the lattice. However, there are eight pivalate ligands where the three methyl groups were refined in two parts each. One of those was refined in three parts and the last one was refined according to an imaginary mirror bisecting the OCO bridge. The protons on the four monodentate

[1] Department of Chemistry, University of Florida, Gainesville, FL 32611, USA
[2] Department of Chemistry, University of California at Davis, Davis, CA 95616, USA
[3] Physical Biosciences Division, Lawrence Berkeley National Laboratory, Berkeley, CA 94720, USA
[*] To whom correspondence should be addressed. E-mail: christou@chem.ufl.edu

pivalic acid ligands were calculated in idealized positions and were refined as riding on their parent O atoms. A total of 807 parameters were refined on F^2 in the final cycle of refinement using 10918 reflections with $I > 2\sigma(I)$ to yield R_1 and wR_2 of 6.35 and 15.75%, respectively.

Table S1. Crystallographic data for complex **1**

Parameter	**1**	Parameter	**1**
formula	$C_{60}H_{112}Ca_2Mn_3O_{28}$	Z	8
fw, $gmol^{-1}$	1526.48	T, °C	173 (2)
crystal system	Monoclinic	radiation, Å [a]	0.71073
space group	*C2/c*	ρ_{calc}, mg/m^3	1.260
a, Å	47.903 (4)	μ, mm^{-1}	0.662
b, Å	15.4607 (11)	Data /restraints /parameters	12592 / 6 / 807
c, Å	23.4133 (17)	Goodness-of-fit on F^2 [b]	1.015
α, deg	90	Reflections Collected	43041
β, deg	111.8440 (10)	*R*1 [c, d]	0.0724
γ, deg	90	*wR*2 [e]	0.1664
V, $Å^3$	16095 (2)	Largest diff. peak and hole, $e*Å^{-3}$	1.779 and -0.805

[a] Graphite monochromator. [b] $S = [\Sigma[w(F_o^2 - F_c^2)^2] / (n\text{-}p)]^{1/2}$. [c] $I > 2\sigma(I)$, $R1 = \Sigma(||F_o| - |F_c||)/\Sigma|F_o|$. [d] $wR2 = [\Sigma [w(F_o^2 - F_c^2)^2]/ \Sigma [w(F_o^2)^2]]^{1/2}$, $w = 1/[\sigma^2(F_o^2) + (m*p)2 + (n*p)]$, where $p = [\max(F_o^2, 0) + 2F_c^2]/3$, *m* and *n* are constants.

Table S2. Bond Valence Sum (BVS) calculations for manganese and selected oxygen atoms in **1**

Mn atom[a]	Mn^{II}	Mn^{III}	Mn^{IV}	O atom	BVS	Assignment[b]
Mn1	4.23	3.87	**4.06**	O1	2.13	O^{2-} (μ_3)
Mn2	4.18	3.82	**4.01**	O2	1.88	O^{2-} (μ_3)
Mn3	4.11	3.77	**3.95**	O3	2.00	O^{2-} (μ_3)
				O4	2.0	O^{2-} (μ_4)
				O14	1.57	OH (pivalic acid)
				O16	1.27	OH (pivalic acid)
				O26	1.20	OH (pivalic acid)
				O28	1.16	OH (pivalic acid)

[a] The values in bold are the one closest to the charge for which it was calculated. The oxidation state is the nearest whole number to the bold value.
[b] Calculated oxygen BVS values for non-, singly-, and doubly protonated O atoms are typically in the ~1.8–2.0, 1.0–1.3, and ~0.2–0.4 ranges, respectively, but can be affected by H-bonding, uncertainties in bond distances due to disorder, etc.

Magnetic Susceptibility Data Collection and Fit

Variable-temperature DC and AC magnetic susceptibility data were collected at the University of Florida using a Quantum Design MPMS-XL SQUID magnetometer equipped with a 7 T magnet operating in the 1.8–300 K range. Samples were embedded in solid eicosane to prevent torquing. Pascal's constants were used to estimate the diamagnetic correction, which was subtracted from the experimental susceptibility to give the molar paramagnetic susceptibility (χ_M).

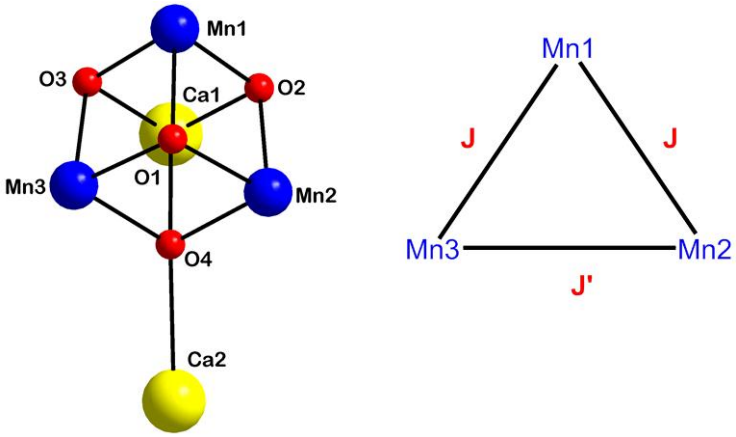

Figure S2. (left) $[Mn_3Ca_2O_4]$ core of **1** from a viewpoint emphasizing the isosceles Mn^{IV}_3 triangular unit; (right) the corresponding 2-*J* coupling scheme and definition of the *J* and *J*′ exchange parameters.

Table S3. Possible S_T spin states for complex **1**.

S_T [a]	n [b]	S_A values
9/2	1	3
7/2	2	3, 2
5/2	3	3, 2, 1
3/2	4	3, 2, 1, 0
1/2	2	2, 1

[a] Twelve total S_T states. [b] Number of states of this S_T value

The Van Vleck equation, where TIP is the temperature independent paramagnetism.

$$X_M = \frac{Ng^2\beta^2}{3kT}\frac{\sum S_T(S_T+1)(2S_T+1)\Omega(S_T)\exp\left[\frac{-E(S_T)}{kT}\right]}{\sum(2S_T+1)\Omega(S_T)\exp\left[\frac{-E(S_T)}{kT}\right]} + \text{TIP} \quad \text{(S1)}$$

EPR Experimental Methods

All EPR samples of complex **1** were dissolved in acetonitrile (ACN) and dichloromethane (DCM) in a 1:1 ratio to a concentration of 1 mM. Perpendicularly polarized CW X-band (9 GHz) spectra were collected using a Bruker model ECS106 spectrometer equipped with a standard mode cavity. All CW X-band spectra were collected at 10 K under non-saturating slow-passage conditions. Temperature control was maintained with an Oxford Instruments model ESR900 helium flow cryostat with an Oxford ITC 503 temperature controller. Q-band (34 GHz) pulsed EPR spectra were acquired with a Bruker EleXsys E580 spectrometer using either an EN 5107D2 Q-band EPR/ENDOR probe or a laboratory–built TE011 brass cavity and coupler following a standard design (2). The laboratory–built probe was also used to acquire the Q-band field swept spectrum. The resonator was modified from previous applications, for an Oxford CF935 cryostat (3). Electron spin echo (ESE)-detected electron nuclear double resonance (ENDOR) spectra were obtained using the Davies ENDOR sequence (π_{MW}-t-π_{RF}-t-$\pi/2_{MW}$-τ-π_{MW}) with stochastic sampling of the RF excitation frequencies (4), and an Amplifier Research model 253 (250 W) RF amplifier. Additional spectrometer settings used were: τ = 230 ns; $\pi/2_{MW}$ = 32 ns; $\upsilon_{MW} \approx$ 34 GHz; RF π-pulse length = 36 μs; t (the delay between microwave and RF pulses) = 1 μs. Additional parameters are listed in Fig. captions. All spectral simulations were performed using Matlab 7.8.0 and the EasySpin 3.1.7 package (5, 6).

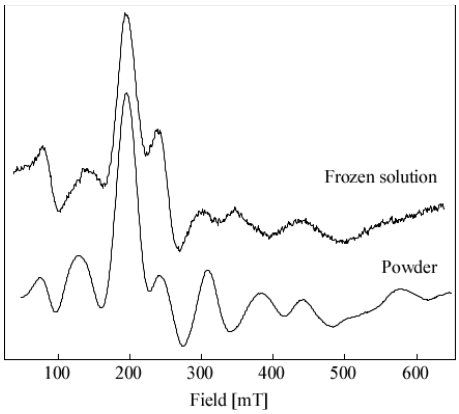

Figure S3. CW EPR of complex **1** dissolved 1:1 ratio of ACN/DCM and the powder. X-band EPR parameters: ν_{MW} = 9.4773 GHz (frozen solution); 9.4805 GHz (powder); microwave power = 6.3 mW; modulation amplitude = 0.8 mT; temperature = 5 K.

The low-temperature (5 K) CW EPR spectrum of a microcrystalline sample of complex **1** possesses almost identical spectral features to those from a sample that has been dissolved into ACN/DCM solvent mixture. This suggests that the electronic structure of the paramagnet is not greatly perturbed by dissolution of the complex (e.g., Figure S3). The 5 K X- and Q-band EPR spectra of a solution of **1** (Figure 6) are characterized by many resonances across a large field range. This is diagnostic of zero-field splittings between the five Kramers doublets of the S_T = 9/2 spin system that are on the order of the microwave excitation energy ($h\nu \approx 0.3$ cm^{-1} and 1.1 cm^{-1}, for X- and Q-band, respectively). Indeed, by simulating both data sets simultaneously, we find that the zero-field splitting constants are D = |0.068| cm^{-1} and E = 0.0052 cm^{-1}.

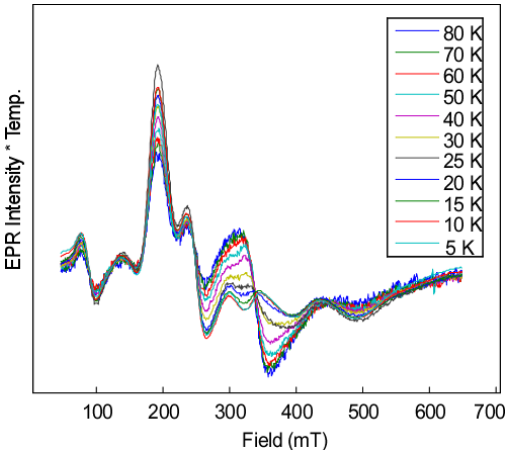

Figure S4. CW EPR temperature dependence of complex **1** at 5, 10, 15, 20, 25, 30, 40, 50, 60, 70 and 80 K; spectra have been scaled by the temperature. Experimental parameters: ν_{MW} = 9.3753 GHz; modulation amplitude =1 mT, microwave power = 1.6 mW.

By increasing the temperature above 5 K, a new derivative-shaped feature grows in centered at 300 mT in the X-band spectrum (Figure S4). We assign this feature to transitions within the excited S_T = 7/2 spin state manifold that becomes thermally populated as the temperature is elevated. This finding is consistent with the exchange coupling scheme described above and in the main body of the paper, which shows the S_T = 7/2 manifold lies only ≈50 cm^{-1} above the S_T = 9/2 ground state.

Figure S5 reveals the ENDOR at different field positions along the EPR envelope of complex **1**. The overlapping EPR transitions are responsible for the variation in peak intensities. This is confirmed by simulations. The asterisk in Figure S5 tracks the proton matrix peak at the various field positions. The

effective hyperfine values determined from simulating the ENDOR at the different fields must be scaled by projection factors to account for the isolated hyperfine interactions. The Mn^{IV} ions in complex **1** have similar coordination environments, as a result the projection factors for each of the isolated ions are assumed to be the same, all equal to 1/3. This is confirmed by applying the relationships used to calculate the projection factors of a trinuclear cluster (7).

c_1 ($S_1S_2S_{12}S_3S$) = c_1 ($S_{12}S_3S$) c_1 ($S_1S_2S_{12}$)

c_2 ($S_1S_2S_{12}S_3S$) = c_1 (S_12S_3S) c_2 ($S_1S_2S_{12}$)

c_3 ($S_1S_2S_{12}S_3S$) = c_2 ($S_{12}S_3S$)

After scaling the effective hyperfine interaction by the projection factor the magnitude of the isolated hyperfine interactions for the two equivalent Mn ions is equal to a = [183, 183, 189] MHz and the third Mn ion is a' = [183,183,171] MHz. This compares well to literature values for Mn^{IV} ions in exchanged coupled systems, refer to Table S4. An in-depth analysis of the magnetic properties of complex **1** will be forthcoming in a subsequent report.

Table S4. ^{55}Mn hyperfine coupling tensors.

	A_{iso} [MHz]	References		A_{iso} [MHz]	References
[Mn^{IV}]	185	This work	**[5]**	207	(10)
[$Mn^{IV'}$]	179	This work	**[6]**	213	(10)
[1]	190	(8)	**[Mn-cat]**	238	(10)
[2]	|183|	(9)	**Mn_4O_xCa**	191-251[a]	(12)
[3]	218	(10)	**Mn_4O_xSr**	173-243[a]	(12)
[4]	221	(11)			

1: $[Mn^{IV}H_3buea(O)]^-$, $[H_3buea]^{3-}$ = tris[*N'*-tert-butylureaylato)-*N*-ethylene]aminato); **2**: $[LMn(\mu\text{-}O)MnL]^{3+}$, L = N,N-bis(2-pyridylmethyl)-*N'*-salicyliden-1,2- diaminoethane); **3**: $[bipy)_2Mn(\mu\text{-}O)_2Mn(bipy)_2]^{3+}$, bipy = 2,2'-bipyridine; **4**: $[(phen)_2Mn(\mu\text{-}O)_2Mn(phen)_2]^{3+}$, phen = 1,10-phenanthroline); **5**: $[(dtne)Mn(\mu\text{-}O)_2(\mu\text{-}OAc)Mn]^{2+}$, dtne = 1,2-bis(1,4,7 – triazacyclonon -1-yl)ethane); **6**: $[(tacn)Mn_2(\mu\text{-}O)_2((\mu\text{-}OAc)(tacn)]^{2+}$, tacn = 1,4,7-triazacyclononane); $[(tacn)Mn_2(\mu\text{-}O)((\mu\text{-}OAc)_2Mn(tacn)]^{3+}$; **Mn-Cat**: manganese catalase; **Mn_4O_xCa** OEC from *T. elongatus*; **Mn_4O_xSr** OEC from *T. elongatus*. [a] The range of effective isotropic hyperfine interaction reported for the three Mn^{IV} ions in the S_2 state of the OEC determined using ^{55}Mn ENDOR at Q-band.

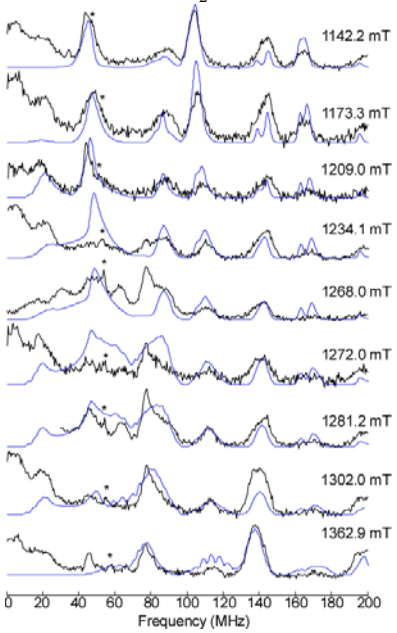

Figure S5. Q-band ^{55}Mn Davies ENDOR of complex **1** taken across the EPR envelope, simulations shown in green. Experimental parameters; τ = 230 ns; $\pi/2_{MW}$ =32 ns; ν_{MW} = 34.186 GHz; microwave power = 1.920 mW; RF pulse length = 36 μs. Asterisks denote the proton matrix peak.

Ca X-ray Absorption Spectroscopy (XAS) Data Collection. The radiation was monochromatized by a Si(111) double-crystal monochromator. Intensity of the incident X-rays was monitored by a He-filled ion chamber (I_0) in front of the sample. XAS samples were made by spreading a very thin layer of finely ground powdered compound on a Ca-free Mylar tape covered with a 6 μm thick polypropylene film. The polypropylene side was directed towards the X-ray beam to reduce attenuation of the X-rays. Samples were placed inside a helium gas-filled bag and cooled with a liquid helium cryostream (Oxford) to ~40 K. Fluorescence spectra were recorded by using a four-element Vortex detector. Energy was calibrated by the edge peak of calcium acetate (4050 eV). Each XANES and EXAFS scan required 17 and 30 minutes to complete, respectively. An X-ray radiation damage study was conducted on each sample prior to data collection by monitoring the Mn K-edge before and after collection of data at the Ca edge. It was determined that it was safe to collect three scans per spot for XANES and two scans per spot for EXAFS with a incoming beamsize of 10 (H) x 2 (V) mm.
Ca X-ray absorption spectra were also measured at beamline 10.3.2 of the Advanced Light Source (ALS), Berkeley operating at electron energy of 1.9 GeV (an average current of 300 mA). The radiation was monochromatized by a Si(111) double-crystal monochromator. Intensity of the incident X-ray was monitored by a He/N_2-filled ion chamber (I_0) in front of the sample. Fluorescence spectra were recorded by using a seven-element Ge detector array. All spectra were collected at room temperature. From a radiation damage study prior to data collection, it was considered safe to collect three scans per spot for XANES and two scans per spot for EXAFS with a spot size of 300 (H) x 20 (V) μm.

Mn XAS data collection. The radiation was monochromatized by a Si(220) double-crystal monochromator. The intensity of the incident X-ray was monitored by an N_2-filled ion chamber (I_0) in front of the sample. XAS samples were made by carefully grinding 5-10 mg of compound and diluting it with a 10-fold excess of boron nitride. The mixture was packed into 0.5-mm-thick sample holders and sealed with Mylar tape. The data were collected as fluorescence excitation spectra with a PIPS detector. Energy was calibrated by the pre-edge peak of $KMnO_4$ (6543.30 eV). The standard was placed between two N_2-filled ionization chambers (I_1 and I_2) after the sample. The X-ray flux at 6.6 keV was between 2 and $5*10^9$ photons $s^{-1}mm^{-2}$ of the sample. Samples were kept at a temperature of 10 K in a liquid helium flow cryostat to minimize radiation damage.

Data reduction and analysis for EXAFS
Data reduction of the EXAFS spectra was performed using EXAFSPAK (Drs. Graham George and Ingrid Pickering, SSRL). Pre-edge and post-edge backgrounds were subtracted from the XAS spectra, and the results were normalized with respect to edge height. Background removal in *k*-space was achieved through a five-domain cubic spline. Curve fitting was performed with Artemis and IFEFFIT software using *ab initio*-calculated phases and amplitudes from the program FEFF 8.2. These *ab initio* phases and amplitudes were used in the EXAFS equation:

$$\chi(k) = S_0^2 \sum_j \frac{N_j}{kR_j^2} f_{eff_j}(\pi,k,R_j) e^{-2\sigma_j^2 k^2} e^{-2R_j/\lambda_j(k)} \sin(2kR_j + \phi_{ij}(k)) \qquad \text{(S2)}$$

The neighboring atoms to the central atom(s) are divided into *j* shells, with all atoms with the same atomic number and distance from the central atom grouped into a single shell. Within each shell, the coordination number N_j denotes the number of neighboring atoms in shell *j* at a distance of R_j from the central atom. $f_{eff_j}(\pi,k,R_j)$ is the *ab initio* amplitude function for shell *j*, and the Debye-Waller term $e^{-2\sigma_j^2 k^2}$ accounts for damping due to static and thermal disorder in absorber-backscatterer distances. The mean free path term $e^{-2R_j/\lambda_j(k)}$ reflects losses due to inelastic scattering, where $\lambda_j(k)$ is the electron mean free path. The oscillations in the EXAFS spectrum are reflected in the sinusoidal term, $\sin(2kR_j + \phi_{ij}(k))$ where $\phi_{ij}(k)$ is the *ab initio* phase function for shell *j*. S_0^2 is an amplitude reduction factor due to shake-up/shake-off processes at the central atom(s). The EXAFS equation was used to fit the experimental data using *N*, *R*, and the EXAFS Debye-Waller factor (σ^2) as variable parameters.

Mn and Ca EXAFS Fits

The EXAFS fitting was carried out using the information about the distances and the coordination numbers obtained from the crystal structure of the Mn_3Ca_2 complex **1**. The fits are shown in Fig. S6. Fig. S6 a) and c) show the comparisons of the Mn and Ca EXAFS of the complex and the best fit. Fig. S6 b) and d) show the Mn and Ca EXAFS FTs of the complex and the best fits.

Mn EXAFS. In Mn EXAFS, the fit quality is satisfactory even with a four-shell fit where only the main interactions were used (Table S5, Fit#1). Addition of light atom contributors such as Mn-O and Mn-C for > 2nd coordination sphere further improved the fit quality (Table S5, Fit#2).

Ca EXAFS. In Ca EXAFS, the fit quality did not improve by the addition of light atom contributors (Table S6, Fit#1 vs Fit#2).

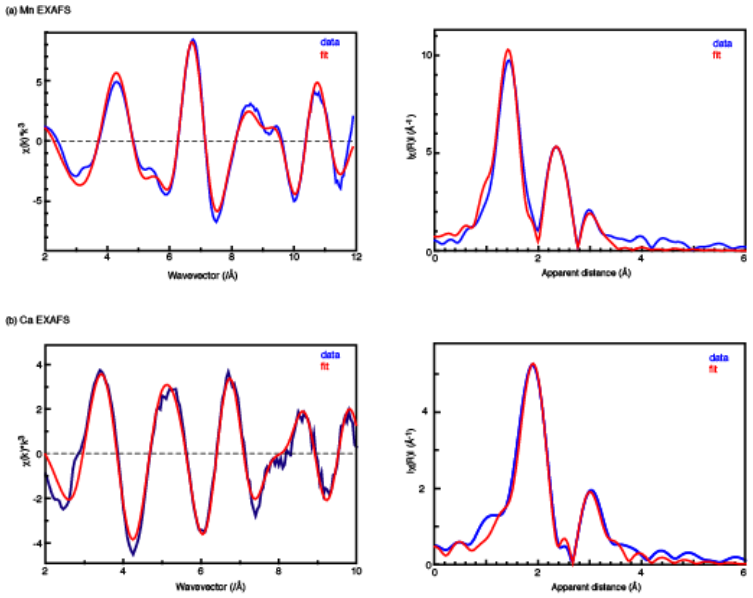

Figure S6. a) and c) are Mn and Ca EXAFS data from **1** and the best fits. b) and d) are the FTs of the Ca EXAFS from the complex and the best fits. The fit parameters are shown in Tables S5 and S6.

Table S5: Mn EXAFS curve fitting for Complex 1

Fit #	Path	R	N	σ^2	R (%)
1	MnO	1.89	**6.0**	0.005	8.2
	MnMn	2.78	**2.0**	0.004	
	MnCa	3.36	**1.0**	0.003	E_0=-6.7
	MnCa	3.78	**0.7**	0.003	
2	MnO	1.89	**6.0**	0.005	5.2
	MnMn	2.75	**1.3**	0.002	
	MnMn	2.88	**0.7**	0.002	E_0=-7.5
	MnC	2.84	**2.7**	0.005	
	MnCa	3.36	**1.0**	0.003	
	MnCa	3.77	**0.7**	0.003	
	MnO	3.05	**3.3**	0.003	

* The data were fit in *k*-space (2.3 – 11.7 /Å). The coordination number (N) was fixed according to the crystal structure. S_0^2 was fixed to 0.85.

Table S6: Ca EXAFS curve fitting for Complex 1

Fit #	Path	R	N	σ^2	R (%)
1	CaO	2.42	**7.0**	0.009	2.4
	CaMn	3.39	**1.5**	0.006	
	CaC	3.14	**5.5**	0.016	E_0=-1.8
	CaMn	3.77	**1.0**	0.018	
2	CaO	2.41	**7.0**	0.009	2.9
	CaMn	3.39	**1.5**	0.007	
	CaC	3.29	**5.5**	0.045	E_0=-2.1
	CaMn	3.77	**1.0**	0.007	
	CaOC	3.56	**10.0**	0.011	
	CaO	3.88	**5.0**	0.014	

* The data were fit in *k*-space (2.9 – 10.0 /Å). The coordination number (N) was fixed according to the crystal structure. S_0^2 was fixed to 0.88.

References

1. SHELXTL6 (2000) (Bruker, AXS, Madison, WI).
2. Sienkiewicz A, Smith BG, Veselov A, Scholes CP (1996) Tunable Q-band resonator for low temperature electron paramagnetic resonance electron nuclear double resonance measurements. *Rev. Sci. Instrum.* 67: 2134-2138.
3. Calvo R, Abresch EC, Bittl R, Feher G, Hofbauer W, Isaacson RA, Lubitz W, Okamura MY, Paddock ML (2000) EPR study of the molecular and electronic structure of the semiquinone biradical Q(A)(-center dot) Q(B)(-center dot) in photosynthetic reaction centers from Rhodobacter sphaeroides. *J. Am. Chem. Soc.* 122: 7327-7341.
4. Epel B, Arieli D, Baute D, Goldfarb D (2003) Improving W-band pulsed ENDOR sensitivity-random acquisition and pulsed special TRIPLE. *J. Magn. Reson.* 164: 78-83.
5. Stoll S, Britt RD (2009) General and efficient simulation of pulse EPR spectra. *PCCP* 11: 6614-6625.
6. Stoll S, Schweiger A (2006) EasySpin, a comprehensive software package for spectral simulation and analysis in EPR. *J. Magn. Reson.* 178: 42-55.
7. Bencini AG (1990) *Electron Paramagnetic Resonance of Exchange Coupled Systems* (Springer, Verlag Berlin Heidelberg New York London Parix Tokyo Hong Kong).
8. Parsell TH, Behan RK, Green MT, Hendrich MP, Borovik S (2006) Preparation and properties of a monomeric Mn-IV-oxo complex. *J. Am. Chem. Soc.* 128: 8728-8729.
9. Horner O, Anxolabehere-Mallart E, Charlot MF, Tchertanov L, Guilhem J, Mattioli TA, Boussac A, Girerd JJ (1999) A new manganese dinuclear complex with phenolate ligands and a single unsupported oxo bridge. Storage of two positive charges within less than 500 mV. Relevance to photosynthesis. *Inorg. Chem.* 38: 1222-1232.
10. Teutloff C, Schafer KO, Sinnecker S, Barynin V, Bittl R, Wieghardt K, Lendzian F, Lubitz W (2005) High-field EPR investigations of $Mn^{III}Mn^{IV}$ and $Mn^{II}Mn^{III}$ states of dimanganese catalase and related model systems. *Magn. Reson. Chem.* 43: S51-S64.
11. Schafer KO, Bittl R, Lendzian F, Barynin V, Weyhermuller T, Wieghardt K, Lubitz W (2003) Multifrequency EPR investigation of dimanganese catalase and related Mn(III)Mn(IV) complexes. *J. Phys. Chem. B* 107: 1242-1250.
12. Cox N, Rapatskiy L, Su JH, Pantazis DA, Sugiura M, Kulik L, Dorlet P, Rutherford AW, Neese F, Boussac A, Lubitz W, Messinger J (2011) Effect of Ca^{2+}/Sr^{2+} Substitution on the Electronic Structure of the Oxygen-Evolving Complex of Photosystem II: A Combined Multifrequency EPR, ^{55}Mn-ENDOR, and DFT Study of the S_2 State. *J. Am. Chem. Soc.* 133: 3635-3648.